



This is a repository copy of *A novel contact interaction formulation for voxel-based micro-finite-element models of bone*.

White Rose Research Online URL for this paper:
<http://eprints.whiterose.ac.uk/130876/>

Version: Accepted Version

Article:

Bhattacharya, P., Betts, D. and van Lenthe, G.H. (2018) A novel contact interaction formulation for voxel-based micro-finite-element models of bone. *International Journal for Numerical Methods in Engineering*, 115 (4). pp. 411-426. ISSN 0029-5981

<https://doi.org/10.1002/nme.5810>

This is the peer reviewed version of the following article: Bhattacharya, P, Betts, D, van Lenthe, GH. A novel contact interaction formulation for voxel-based micro-finite-element models of bone. *Int J Numer Methods Eng*. 2018; 115: 411– 426., which has been published in final form at <https://doi.org/10.1002/nme.5810>. This article may be used for non-commercial purposes in accordance with Wiley Terms and Conditions for Use of Self-Archived Versions.

Reuse

Items deposited in White Rose Research Online are protected by copyright, with all rights reserved unless indicated otherwise. They may be downloaded and/or printed for private study, or other acts as permitted by national copyright laws. The publisher or other rights holders may allow further reproduction and re-use of the full text version. This is indicated by the licence information on the White Rose Research Online record for the item.

Takedown

If you consider content in White Rose Research Online to be in breach of UK law, please notify us by emailing eprints@whiterose.ac.uk including the URL of the record and the reason for the withdrawal request.



eprints@whiterose.ac.uk
<https://eprints.whiterose.ac.uk/>

A novel contact interaction formulation for voxel-based micro-finite-element models of bone

P. Bhattacharya^{1,2*}, D. Betts³ and G. H. van Lenthe¹

¹*KU Leuven – University of Leuven, Department of Mechanical Engineering, Biomechanics Section,
Celestijnenlaan 300C, bus 2419, 3001 Leuven, Belgium*

²*Insigneo Institute for in silico Medicine and Department of Mechanical Engineering, University of Sheffield, Pam
Liversidge Building, Mappin Street, Sheffield S1 3JD, United Kingdom*

³*ETH Zürich, Institut für Biomechanik, HCP H 22.2, Leopold-Ruzicka-Weg 4, 8093 Zürich, Switzerland*

SUMMARY

Voxel-based micro-finite-element (μ FE) models are used extensively in bone mechanics research. A major disadvantage of voxel-based μ FE models is that voxel surface jaggedness causes distortion of contact-induced stresses. Past efforts in resolving this problem have only been partially successful; i.e., mesh smoothing failed to preserve uniformity of the stiffness matrix, resulting in (excessively) larger solution times, whereas reducing contact to a bonded interface introduced spurious tensile stresses at the contact surface. This paper introduces a novel ‘smooth’ contact formulation that defines gap distances based on an artificial smooth surface representation while using the conventional penalty contact framework. Detailed analyses of a sphere under compression demonstrated that the smooth formulation predicts contact-induced stresses more accurately than the bonded contact formulation. When applied to a realistic bone contact problem, errors in the smooth contact result were under 2%, whereas errors in the bonded contact result were up to 42.2%. We conclude that the novel smooth contact formulation presents a memory-efficient method for contact problems in voxel-based μ FE models. It presents the first method that allows modeling finite slip in large-scale voxel meshes common to high-resolution image-based models of bone while keeping the benefits of a fast and efficient voxel-based solution scheme. Copyright © 2010 John Wiley & Sons, Ltd.

Received ...

1. INTRODUCTION

1 Micro-computed-tomography (μ CT) images of bone, discretized on a Cartesian grid, can be used
2 directly to define a micro-finite-element (μ FE) model where each volume element (henceforth
3 voxel) has an identical cubic shape. Over the last three decades, voxel-based μ FE models have
4 been used to perform non-invasive biomechanical investigations [1, 2, 3]. Recent advances in
5 using highly-parallelized multi-grid solvers have made it possible to rapidly solve voxel-based μ FE
6 models with millions of degrees of freedom (DOFs) [4]. The advent of voxel-based μ FE models
7 have not only revolutionized healthcare technology at the point-of-care (e.g. HRpQCT-based bone
8 strength analysis [5]) but have also pushed the frontiers of exploitation of imaging techniques
9 (Synchrotron Radiation CT-imaging [6]). Voxel-based μ FE modelling is perhaps indispensable
10 in studying bone-remodelling within cancellous tissue since it possesses the necessary level of
11 microstructural fidelity in comparison to homogenized continuum FE models [7, 8].

12 In voxel-based μ FE models all voxel edges are oriented along the same Cartesian axes.
13 These models fail to smoothly discretize any surface that has an orientation different from
14 the three Cartesian directions. A natural surface, e.g., of a bone, thus becomes jagged in the
15 voxel representation and causes artificial stress and traction concentrations. To overcome this
16 problem, researchers have investigated the effect of smoothing the surface by distorting the
17 voxels [9, 10, 11, 12]. Using a model of a two-dimensional (2D) annular ring it has been shown
18 that smoothing, but not mesh refinement, reduces the error in the predicted stresses [11]. However,
19 mesh smoothing increases computing costs as the stiffness matrix for each distorted element must
20 be computed individually. For example, in a model of trabecular bone microstructure the application

*Correspondence to: Insigneo Institute for *in silico* Medicine and Department of Mechanical Engineering,
University of Sheffield. Pam Liversidge Building, Mappin Street, Sheffield S1 3JD, United Kingdom. E-mail:
p.bhattacharya@sheffield.ac.uk. Phone: +44 114 222 6174.

21 of smoothing to voxel-based meshes did not result in a significant reduction of stresses on the bone
22 surfaces compared to the substantial increase in simulation times [9, 10].

23 For problems involving contact, the error is further influenced by a modelling artifact related
24 to the orientation of the voxel relative to the loading direction [13]. Quantification of the contact-
25 induced errors in stress prediction accounting for voxel orientation, is yet to be performed. The
26 error in the predicted stress at the boundary becomes critical in models where contact is present.
27 A common approach is to ‘bond’ the opposing surfaces [14, 15, 3, 16]. By design, this method is
28 not suitable in situations where node contact pairs are changing during the simulation: e.g. incipient
29 contact, secondary instability and finite sliding. Hence, this bonding approach has been restricted
30 to some limited scenarios of loading at the bone–implant interface. Though the global strength [3]
31 and apparent stiffness [14] of the bone–implant bond have been satisfactorily predicted by this
32 approach, the quality of local stress prediction remains unknown. Furthermore, tensile tractions can
33 be predicted which obviously cannot occur in physical reality.

34 In standard FE, the node-to-surface contact formulation [17, 18] has been widely used to model
35 three-dimensional (3D) contact interaction. In this formulation, one of the two contacting surfaces
36 (the ‘master’ surface) possesses a higher stiffness, lower mesh refinement, lesser degrees of freedom,
37 or a combination of these, compared to the opposing (‘slave’) surface. The orientation of voxels
38 edges and the shape of the voxels at the slave surface do not influence the contact formulation. Only
39 the separation distance of slave-surface nodes relative to the master surface elements determines the
40 contact stresses.

41 The aim of this paper is to develop an efficient contact algorithm that can take full advantage
42 of voxel-based meshes. We hypothesize that the contact-induced stresses can be quantified using
43 the penalty-based contact formulation from standard FE, while redefining the distance between
44 slave nodes relative to the master surface based on an artificially defined surface that does not alter
45 the shape of the voxels. The paper introduces a ‘smooth’ contact formulation in which the node-
46 to-surface formulation is modified by defining ghost slave nodes that lie on a nominally smooth
47 surface. The problem of elastic compression of a sphere is analyzed using voxel-based models. This

48 problem is the 3D counterpart of the elastic compression of an infinitely long cylinder in 2D [19,
 49 p. 107]. The sphere model allows the investigation of contact-induced errors in dependence of mesh
 50 refinement and relative voxel orientation without other confounding factors. The effectiveness of
 51 the novel smooth contact formulation is demonstrated further by analysing the realistic problem of
 52 contact in a human hip joint between the femur and the acetabulum.

2. METHOD

53 2.1. Finite-element discretization and contact formulations

54 In the standard FE approach [18, 20, 21] a contact problem is expressed by the matrix equation

$$0 = \mathbf{F} + \mathbf{R}^c - \mathbf{K}\mathbf{a} \quad (1)$$

55 where \mathbf{K} is the stiffness matrix, \mathbf{F} , \mathbf{R}^c and \mathbf{a} are the vectors of applied forces, contact forces and
 56 nodal displacements, respectively. In the penalty contact enforcement method, the contact force \mathbf{R}^c
 57 is related to the contact gap between the opposing contact surfaces through a contact-interaction
 58 law. For example, a hard–frictionless contact is specified as

$$\mathbf{R}^c = \begin{cases} -k_c g_n \mathbf{n} & g_n < 0 \\ 0 & \text{otherwise} \end{cases} \quad (2)$$

59 Here a node-to-surface discretization is used, with one contact surface defined as the master and the
 60 opposite surface defined as the slave. The contact force acting on any node of the slave surface is
 61 given by \mathbf{R}^c above, k_c is a constant scalar referred to as the penalty stiffness parameter, the contact
 62 gap is defined as $g_n \equiv \mathbf{n} \cdot (\mathbf{s} - \mathbf{m})$, \mathbf{n} is the current outward normal to the master facet closest to the
 63 slave node, \mathbf{s} is the current position of the slave node and \mathbf{m} is the current position of a node on the
 64 closest master facet. Equal and opposite contact forces are distributed on nodes of the master facet.
 65 For nodes that do not belong to either the master or slave surfaces, the contact force is zero.

66 The set of equations (1) and (2) is non-linear in \mathbf{a} , since \mathbf{R}^c , g_n and \mathbf{n} depend on \mathbf{a} through
 67 their dependence on current nodal positions. To determine the unknowns \mathbf{a} and \mathbf{R}^c , one attempts to

68 iteratively minimize the residual

$$\mathbf{r} = \mathbf{F} + \mathbf{R}^c - \mathbf{K}\mathbf{a} \quad (3)$$

69 Using Δ to denote a variation between successive iterations, linearization of Eqs. (2) and (3) gives

$$\Delta \mathbf{R}^c = -\mathbf{K}^c \Delta \mathbf{a} \quad (4)$$

$$\Delta \mathbf{r} = \Delta \mathbf{R}^c - \mathbf{K} \Delta \mathbf{a} \quad (5)$$

70 where \mathbf{K}^c is the so-called contact stiffness matrix. The displacement update that minimizes the
71 residual (i.e. $\mathbf{r} + \Delta \mathbf{r} = 0$) is obtained by combining Eqs. (3)–(5), to get

$$\Delta \mathbf{a} = (\mathbf{K} + \mathbf{K}^c)^{-1} (\mathbf{F} + \mathbf{R}^c - \mathbf{K}\mathbf{a}) \quad (6)$$

72 The updates are iteratively computed and applied to \mathbf{a} until convergence is reached. This
73 conventional formulation is henceforth referred to as the Stair-Case, Sliding Contact (SC-SC)
74 model, where ‘stair-case’ highlights the jaggedness of the voxelated slave surface, and ‘sliding
75 contact’ highlights that slave node displacement tangential to the master surface is not restricted. We
76 note that the entire treatment is a standard approach and has been discussed in detail in textbooks
77 on the subject [18].

78 In the smooth contact formulation, each slave node is identified with a ghost slave node, where
79 the ghost slave nodes lie on a smooth representation of the voxelated slave surface in the reference
80 configuration. It is not needed to discretize the smooth representation of the voxelated surface into
81 finite surface elements, and one may identify the ghost slave node as the position on the smooth
82 representation of the voxelated surface that is closest to the slave node in the SC-SC model. Identical
83 displacements are applied to the slave node and its corresponding ghost slave node at all times. The
84 only difference in the smooth contact formulation with respect to the SC-SC model is that the
85 contact gap is redefined as $g_n \equiv \mathbf{n} \cdot (\tilde{\mathbf{s}} - \mathbf{m})$ where $\tilde{\mathbf{s}}$ is the ghost slave node position in the current
86 configuration. This redefinition modifies the computed contact force vector \mathbf{R}^c and the contact
87 stiffness matrix \mathbf{K}^c , but only up to their dependence on the contact gap distance g_n . This smooth
88 contact formulation is henceforth referred to as the Simulated Smoothed surface, Sliding Contact
89 (SS-SC) model. ‘Simulated smoothed surface’ highlights that ghost slave nodes lying on a fictitious

90 smooth surface are employed in defining the gap distance, but also that this redefinition is the only
91 difference with respect to the SC-SC model. In particular, the voxels connected to slave nodes are
92 not deformed, and the stiffness matrix \mathbf{K} is identical for the SC-SC and SS-SC formulations. The
93 novelty of our method is that an artificial surface is defined that is used to calculate gap distances
94 while the voxelated nature of the elements is kept such that fast and highly memory efficient solvers
95 can be used.

3. APPLICATION TO ELASTIC COMPRESSION OF A SPHERE

96 Consider a deformable sphere (radius R) with its centre at the origin O . In the reference
97 configuration the sphere is stress-free and positioned between two parallel rigid planes that are
98 touching the sphere. We consider the problem where the distance between the rigid planes reduces
99 by $0.2R$ leading to 10 % apparent compressive strain in the sphere.

100 3.1. Voxel models

101 Define a rectangular coordinate system (x, y, z) with the origin located at O and with the direction
102 x aligned along the sphere diameter normal to the rigid contact planes. A reduced form of the
103 above problem is considered by noting that irrespective of the choice of voxelation procedure, the
104 problem is symmetric about the equatorial plane $x = 0$. Hence only the hemispherical region and
105 the one rigid plane lying in the half-space $x \geq 0$ is considered. In this reduced model the surface
106 of the hemisphere initially at $x = 0$ always remains planar but displaces a distance of $0.1R$ in the
107 $+x$ -direction. The rigid plane is held fixed in space.

108 The hemispherical volume is populated by 8-noded linear voxels (side length $a < R$) with edges
109 aligned to a coordinate system (X, Y, Z) with origin at O . The choice of X, Y and Z directions is
110 made as follows. We note that the orientation of the voxels of the hemisphere relative to the rigid
111 contact plane is determined by the orientation of the (X, Y, Z) system relative to the (x, y, z) system.
112 However, due to cubic symmetry of the voxels, only part of the voxelated hemisphere boundary
113 presents unique voxel orientations to a locally tangent plane (shaded region in Figure 1A). It is easy

114 to see that in two dimensions this is equivalent to the fact that only a 45° sector of a pixelated circle
115 presents unique orientations to a locally tangent segment (Figure 1B). Hence locations labeled Loc-
116 1 to Loc-7 are identified within the shaded region (Figure 1A) in order to investigate contact-induced
117 errors in dependence of relative voxel orientation. Coordinates of these locations in the (X, Y, Z)
118 system are listed in Table I. The directions of the coordinate axes (X, Y, Z) are selected such that
119 the locations Loc- i ($i = 1 \dots 7$) in the (X, Y, Z) -system corresponds to the location $(R, 0, 0)$ in the
120 (x, y, z) -system and the Y axis lies anywhere on the x - y plane.

121 Voxeling the hemisphere in the above manner ensures that all voxels possess at least one
122 node for which $x \geq 0$. A flat equatorial surface is obtained by setting $x = 0$ for nodes with
123 $x < 0$. To model the rigid contact plane, a 4-noded rectangular surface element is defined
124 with nodes located at $x = R + g_0$, $y = \pm 0.5R$, $z = \pm 0.5R$. The nominal gap $g_0 = 2a$ between
125 the hemisphere and the rectangular element ensures that penetration does not occur in the
126 reference configuration, irrespective of the choice of voxel size and orientation. In all, 42 different
127 voxel geometries are analysed. In these models the relative orientation between (X, Y, Z) and
128 (x, y, z) coordinate systems varies from Loc-1 to Loc-7 and mesh refinement a/R varies as
129 0.0125, 0.025, 0.0375, 0.05, 0.075 and 0.1 (Figure 2).

130 In all models the hemisphere is considered to be homogeneous isotropic linear elastic with
131 Young's modulus $E = 10$ GPa and Poisson's ratio $\nu = 0.3$. To achieve 10% apparent compressive
132 strain, all nodes of the hemisphere located at $x = 0$ in the reference configuration are displaced by
133 $0.1R + g_0$ in the $+x$ -direction. The y - and z -degrees of freedom (DOFs) of the node at O and the
134 z -DOF of the node nearest to $(0, 0.5R, 0)$ are constrained throughout the solution, thus restricting
135 rigid-body translation and rotation. All nodes of the rectangular surface element are held fixed in
136 space. The total displacement is applied over 10 equal increments.

137 Nodes on the hemisphere surface with $x > 0.9R$ are defined as slave nodes. To simulate bonded
138 contact, all degrees of freedom are restricted for all the slave nodes. For SS-SC models, each slave
139 node position in the reference configuration is projected in the radial direction on the surface of
140 the analytical hemisphere to obtain the corresponding ghost slave node position in the reference

141 configuration. For both SC-SC and SS-SC, hard–frictionless contact interaction is modelled between
142 slave nodes and the master surface (rectangular surface element). The penalty contact stiffness
143 parameter is taken to be $k_c = 0.1ER$ for all models and this was found to result in negligible
144 overclosure. Contact iterations are assumed to have converged if either the maximum absolute
145 difference in nodal displacements between the current contact iteration and the last contact iteration
146 is less than 0.01% of the maximum absolute difference in nodal displacements between the current
147 contact iteration and the last converged increment, or a maximum 10 contact iterations have been
148 performed. The FE models are analyzed using an in-house FE code developed and executed with
149 MATLAB version 8.5.0 (R2015a) (The Mathworks Inc., Massachusetts, United States). Computed
150 results are visualized using software ParaView version 4.3.1 (Kitware Inc., New York, United
151 States).

152 3.2. Benchmark model

153 The benchmark model of the problem is created using a geometry conforming mesh. Axisymmetry
154 reduces the problem to a plane of revolution (Figure 3). The centre of the sphere O coincides with
155 the origin of the planar coordinate system (ξ, ρ) . The axis of revolution is ξ and only the quadrant
156 $\xi, \rho \geq 0$ is considered.

157 The 2D domain of the hemisphere cross section is meshed using 4-noded linear axisymmetric
158 elements with increasing refinement closer to the contact region (element size $\sim 0.005R$). The rigid
159 contact plane is represented by a line segment parallel to the ρ axis and passing through $(R, 0)$. The
160 contact line segment is treated as an analytical solid and is thus not discretized. In the reference
161 configuration the hemisphere and the rigid plane are just in contact.

162 The hemisphere possesses identical constitutive behavior as the voxel-based models. To achieve
163 10% apparent compressive strain, the nodes at the top of the hemisphere are given a displacement
164 of $0.1R$ in the $+\xi$ -direction, while nodes situated on the ξ -axis are constrained from movement in
165 the ρ -direction. The contact line segment is held fixed in space. Hard–frictionless contact behavior
166 using penalty contact enforcement method is implemented using the node-to-surface formulation

167 and with the identical numerical value for k_c as in the voxel models. The hemisphere boundary
168 nodes are defined as slave nodes and the contact line segment acts as master surface. The model is
169 solved using software Abaqus/Standard version 6.13-1 (Dassault Systèmes Simulia Corp., Rhode
170 Island, United States).

4. APPLICATION TO THE HUMAN HIP JOINT

171 Grosland et al. [22] considered the problem of compressive contact at the human hip joint between
172 the femur and the acetabulum. In this paper we considered the same problem, except that: (a) bone
173 geometries are taken from the public data repository of the VAKHUM project [23, 24], (b) a smaller
174 subset of the proximal femur volume is analyzed, (c) a displacement-control boundary condition is
175 applied to the femur (instead of a load-control boundary condition being applied to the pelvis), and
176 (d) the meshing and contact interaction details are as described below. Stereolithography (STL) files
177 for the segmented surfaces of a left femur and a pelvis were downloaded from the repository. Only
178 a subset of the pelvis STL in the region near the acetabulum are retained (61801 facets attached to
179 33477 nodes). The STL for the femur is also cropped to retain triangular facets only in the head
180 region. Additional geometric features (edges and surfaces) are generated to define a closed volume
181 of the femoral head region. Following Grosland et al. [22], a rigid–deformable contact scenario is
182 considered, whereby the pelvis is considered a rigid body and the femur is deformable. Pelvis STL
183 facets are directly used for the surface definition and no volume mesh or material definitions are
184 added. In the reference configuration the femur and pelvis regions do not inter-penetrate and the
185 average contact gap in the acetabular region is ~ 1.5 mm.

186 4.1. Voxel models

187 The voxel model for the above problem is created as follows. The image data from the VAKHUM
188 dataset used a reference coordinate system in which the axes were aligned nominally with the
189 anatomical body axes. The same rectangular coordinate system is used here, hence the x , y and
190 z directions are parallel to the medial–lateral, anterior–posterior and inferior–superior directions

191 respectively. The closed volume of the femur head is discretized using a freely available mesh
192 voxelation package [25]. A total of 55962 linear voxels (side length 1 mm) and 61832 nodes are
193 generated. All voxels possessed linear isotropic elastic material properties ($E = 10$ GPa, $\nu = 0.3$).
194 A displacement, with medial and superior components equal to 3 mm, is applied to all nodes on
195 the lateral and inferior planar surfaces of the femur. For one node on each of these two surfaces,
196 the anterior–posterior displacement component is set to zero in order to prevent spurious rigid body
197 motion.

198 In the bonded contact model, the pelvis STL is used to identify a subset of the femur surface
199 nodes which are to be ‘bonded’. Specifically, femur surface nodes within $3\sqrt{2}$ mm (= magnitude of
200 applied displacement) of the nearest pelvis facet in the reference configuration are selected. Once
201 these ‘bonded’ nodes are identified, the pelvis geometry is discarded, and the ‘bonded’ nodes are
202 held fixed for the rest of the analysis. The displacement of the lateral and inferior planar surfaces of
203 the femur is applied over a single increment.

204 In the SC-SC model, all pelvis facet nodes are held fixed in space. Hard-frictionless contact
205 behavior using a node-to-surface discretization is defined between the femur and the pelvis models.
206 All facets of the pelvis models are considered to be potential master surface facets. Exterior nodes
207 of the femur voxel mesh that are on the acetabulum-facing side of a plane (Figure 4) are defined
208 as slave nodes because only these are likely to come into contact. In the SS-SC model, ghost slave
209 node positions in the reference configuration are defined by projecting the slave nodes of the SC-SC
210 model on to the nearest facet of the femur STL. The total displacement of the femoral head is applied
211 over 5 equal increments. Within each increment, contact is considered between a slave node/ghost
212 slave node (SC-SC/SS-SC) and all those master facets which have at least one node within 4 mm
213 of the current slave node/ghost slave node position. A penalty contact stiffness of $k_c = 1$ GPa.mm
214 was found to result in negligible overclosure. Contact iterations are assumed to have converged
215 if either the maximum absolute difference in nodal displacements between the current contact
216 iteration and the last contact iteration is less than 0.01% of the maximum absolute difference in
217 nodal displacements between the current contact iteration and the last converged increment, or if

218 a maximum 10 contact iterations have been performed. All voxel models are analysed using the
219 in-house finite-element code noted previously.

220 4.2. Benchmark model

221 The coordinate axis system of the benchmark model is identical to that of the voxel models. A
222 tetrahedral mesh is used to discretize the femur head volume using Ansys ICEM CFD 15.0 (ANSYS
223 Inc., Pennsylvania, United States) thus generating 137854 nodes and 788620 linear tetrahedra
224 (nominal element size 1 mm). The triangulated pelvis surface possessed the same rigid body
225 definition as in the voxel models.

226 The femur volume is given identical material properties as in the voxel models. The boundary
227 conditions applied on the femur and pelvis are identical to that in the voxel models. General contact
228 interaction (surface-to-surface contact formulation) is defined between all surface elements of the
229 femur and the pelvis models. Hard–frictionless contact behavior is simulated using the penalty
230 method and an identical value of penalty stiffness k_c as in the voxel models. The benchmark model
231 is solved incrementally, with the total displacement being applied over 5 equal increments. The
232 model is analysed using Abaqus/Standard.

233 4.3. Analysis

234 Computed results are visualized using ParaView. Qualitative comparison of contact-induced stresses
235 between the benchmark and the voxel models is performed by considering stress distributions on a
236 coronal plane of the femoral head plotted in the undeformed configuration. Quantitative comparison
237 of the voxel models with respect to the benchmark model is performed by considering all voxel
238 nodal locations.

5. RESULTS

239 5.1. Elastic compression of sphere

240 As an illustrative result, in Figure 5 the minimum principal stress contours (normalized by E) are
241 plotted on the $y = 0$ plane (reference configuration) for the bonded, SC-SC and SS-SC models, for
242 a representative mesh refinement and voxel orientation ($a/R = 0.075$, Loc-1). In the bonded model,
243 the peak compressive stress occurs at the corners of the bottom-most voxels. This peak compressive
244 stress is also significantly larger in magnitude than the peak compressive stress in the SC-SC and
245 the SS-SC models. Although the peak compressive stress magnitudes are similar in the SC-SC and
246 SS-SC models, the location of the peak compressive stress is more realistic for the SS-SC model
247 than in the SC-SC model. Thus for this representative case, the bonded model predicts both the
248 location and the magnitude inaccurately, the SC-SC model predicts the location inaccurately, while
249 the SS-SC model performs the best of all three.

250 Now considering the results in more detail, stresses and distances are normalized by E and R
251 respectively. Results are reported as a function of the distance along the x (or ζ for benchmark) axes
252 in the undeformed configuration. The normalized distances 0 and 1 correspond respectively to the
253 hemisphere center and the point of nominal contact initiation ($R, 0, 0$). Figure 6A shows all three
254 principal stresses in the benchmark model. The highest compressive stress at any point, and thereby
255 the minimum principal stress direction, is expectedly along x which is the direction of loading. The
256 middle and the maximum principal stresses at any point (Figure 6A) are identical as a consequence
257 of axisymmetry. For the sake of brevity, mid-principal stresses are omitted from further analysis. In
258 the region $x/R \lesssim 0.63$ the maximum principal stress is tensile due to the Poisson's effect in which
259 compression along x causes a radially outward stretch in the $y-z$ plane. Figures 6B, C compare
260 the maximum and minimum principal stresses respectively between the benchmark and the voxel
261 models with $a/R = 0.075$ and orientation Loc-1. The maximum principal stress in these particular
262 voxel models compares better with the benchmark than the minimum principal stress. The maximum
263 error in any contact formulation is expectedly the largest at the point of contact. The magnitude of

264 this largest error is nearly the same for the bonded and SC-SC formulations, and is minimized for
 265 SS-SC.

266 In the following we focus on the region close to the contact surface ($x/R \geq 0.8$). Figure 7
 267 considers principal stresses in dependence of orientation and contact formulation for the coarsest
 268 ($a/R = 0.1$) and the most refined ($a/R = 0.0125$) mesh models. The dispersion across the different
 269 voxel orientations reduces as the mesh is refined irrespective of the choice of contact model. As
 270 the mesh is refined, variation reduces at nearly every location along the radial line, along with a
 271 reduction in extent of the region of large variations. The overall variation in minimum principal
 272 stress is larger than the variation in maximum principal stress for all contact models. For the bonded
 273 contact formulation (Figure 7A, D) the average error, i.e. the difference between the centerline of the
 274 dispersion envelope and the benchmark, does not change significantly due to mesh refinement. This
 275 result is true for either principal stress. For SC-SC (Figure 7B, E) the average errors are significantly
 276 reduced compared to bonded contact, and the reduction is higher for the most refined mesh models.
 277 Yet, the maximum widths of the dispersion envelopes, which occur close to the point of contact,
 278 are substantially larger in SC-SC compared to those in bonded contact for both mesh refinements.
 279 Thus, going from bonded to SC-SC, the accuracy is improved, but the precision is poorer. In
 280 contrast, when SS-SC is used (Figure 7C, F), both the average error and the maximum dispersion
 281 are reduced compared to bonded contact – irrespective of mesh refinement or principal stress being
 282 considered. Thus both accuracy and precision improve in SS-SC when compared to bonded contact.
 283 Increasing mesh refinement leads to an increase in accuracy everywhere, but precision increases
 284 nearly everywhere except in a very small region close to contact.

285 Next, for each principal stress component the normalized maximum absolute error
 286 (NMAXABSE) was quantified as a local error measure:

$$\text{NMAXABSE} = \frac{\max_{i \in [1, N]} |\sigma_i - \tilde{\sigma}_i|}{\max_{i \in [1, N]} |\sigma_i|} \quad (7)$$

287 For each stress component the normalized root mean square error (NRMSE) was defined as a global
 288 error measure as follows:

$$\text{NRMSE} = \frac{\sqrt{\text{avg}_{i \in [1, N]} (\sigma_i - \tilde{\sigma}_i)^2}}{\max_{i \in [1, N]} |\sigma_i|}. \quad (8)$$

289 where σ and $\tilde{\sigma}$ are the principal stress variable obtained from the benchmark and a voxel-based
 290 model respectively. The subscript i is the index of $N = 100$ equispaced points along $x/R \geq 0.8$
 291 where the stresses are evaluated. The normalization factor in the denominator is effectively the
 292 value of the principal stress variable at the point of contact.

293 For a specific combination of mesh refinement, contact model and principal stress variable, both
 294 NMAXABSE and NRMSE depend on voxel orientation. We assume that for an arbitrary orientation
 295 the predicted stress would lie wholly within the envelope of predicted stress values corresponding
 296 to the seven orientations considered here. With this assumption we obtain the maximum and
 297 minimum values of NMAXABSE and NRMSE across all orientations. A larger difference between
 298 the maximum and minimum values is taken to render the local (NMAXABSE) or global (NRMSE)
 299 prediction less precise. A larger average of the maximum and minimum values is taken to render the
 300 local or global prediction less accurate. For the bonded contact models, considering any principal
 301 stress, no significant change in local precision or local accuracy is observed as a function of mesh
 302 refinement (Figures 8A,D). At any given refinement, local precision and local accuracy are similar
 303 between maximum and minimum principal stresses.

304 For SC-SC models (Figures 8B,E), considering any principal stress, mesh refinement does not
 305 improve the local precision, but local accuracy increases for maximum principal stress while it
 306 remains nearly unchanged for minimum principal stress. Minimum principal stress predictions
 307 are less accurate and less precise locally than maximum principal stress predictions for a given
 308 refinement. Comparing with bonded contact, the local accuracy in SC-SC is higher for both principal
 309 stresses at any given mesh refinement. However, the local precision is poorer in SC-SC than in
 310 bonded contact, and especially so in the case of the minimum principal stress.

311 For SS-SC models (Figures 8C,F), considering any principal stress, mesh refinement does
 312 not change the local precision, but local accuracy increases for both principal stresses. At any

313 given refinement, local precision and local accuracy are similar between maximum and minimum
314 principal stresses. Comparing with bonded contact, local accuracy is higher in SS-SC for both
315 principal stresses at any given mesh refinement. Most importantly, this improvement does not
316 adversely affect local precision, which is similar between SS-SC and bonded contact for both
317 principal stress.

318 All the above trends hold when considering global accuracy and precision. We draw attention to
319 the fact that for a given combination of mesh-refinement, contact model and principal stress, both
320 accuracy and precision are higher globally than locally. This highlights that the errors in predicted
321 stresses are localized to the near-contact region.

322 5.2. Femur–acetabulum contact

323 Figure 9 compares the principal stress distribution on a coronal plane between the benchmark,
324 bonded, SC-SC and SS-SC models. The errors in the bonded contact results compared to the
325 benchmark model are substantial and even qualitative agreement is not achieved. Qualitatively, the
326 SC-SC and the SS-SC results agree with the benchmark; but quantitatively, the SS-SC results are
327 superior to the SC-SC results. For example, in the SC-SC results compressive stresses (negative
328 value contours) are concentrated at corners of the boundary, an artifact that is avoided in the SS-SC
329 results. Similarly, regions of negative valued principal stress contours are larger in SC-SC results
330 than in the benchmark and the SS-SC results. This improves both near-surface and interior stress
331 predictions for the SS-SC formulation compared to the SC-SC formulation.

332 The local (NMAXABSE) and global (NRMSE) accuracy in the prediction of principal, normal
333 and shear stresses are compared between the different contact formulations in table II. These error
334 measures were defined previously in Eqs. (7) and (8). For the hip contact problem, the stresses
335 are evaluated at $N = 56313$ points, indexed $i = 1 \dots N$, in the interior of the voxel models and
336 the benchmark model. These points correspond to nodal positions of the voxel models. Due to
337 differences in discretization between the voxel models and the benchmark model, 5519 (= 61832 –
338 56313) voxel nodal positions fall outside the femoral volume of the benchmark model, and are

339 omitted from the error analysis. Although only one voxelation direction was considered, it is noted
340 that the relative orientation of the femur voxel edges and the pelvis facets varies over a large range of
341 angles. This is a result of the highly conforming contact situation that naturally arises in this realistic
342 problem. Hence, unlike in the sphere contact problem, the results here are not expected to change
343 significantly with voxelation direction. It is found that the local accuracy increases going from SC-
344 SC to SS-SC formulations for most stress invariants and components. The local accuracy for bonded
345 contact is always and significantly worse than that for SS-SC. Global accuracy increases by an order
346 of magnitude going from bonded contact to SC-SC, and by yet another order of magnitude when
347 using SS-SC formulation. This highlights that the errors in predicted stresses are spread throughout
348 the femoral head volume. For all the stress variables considered, global errors are up to 42.2% for
349 the bonded model, but only up to 1.16% for the SS-SC model.

6. DISCUSSION AND CONCLUSIONS

350 The jagged surface nature of voxel-based FE models prevents an accurate determination of stresses
351 for a body in contact. Considering first the simple problem of elastic compression of a sphere,
352 it was shown that voxel models exhibited spurious stress concentrations at and near the region
353 of contact. Errors were found to depend on voxel orientation, mesh refinement, choice of contact
354 model and stress variable itself. With increasing mesh refinement, the accuracy of stress prediction
355 was unchanged for bonded contact. Compared to the bonded contact results, accuracy was higher
356 for both SC-SC and SS-SC, and even improved in general with increasing mesh refinement.
357 However, SS-SC performed significantly better than SC-SC in increasing the precision across voxel
358 orientations. The precision in SC-SC was similar or worse than that in bonded contact, and remained
359 nearly unchanged with increasing mesh refinement. In a strong contrast, the precision in SS-SC was
360 similar or smaller than that in bonded contact, and decreased with increasing mesh refinement. Thus
361 the advantage of mesh refinement is expected only in the presence of SS-SC.

362 In the human hip joint contact problem, the femoral head had an overall radius of curvature
363 of about 25 mm, but possessed some local features with radii of curvature down to about 5 mm

364 (visual estimates). Additionally, in this problem nearly all possible voxel orientations relative to
365 the pelvis contact surface were realized due to the highly conforming contact situation. In light of
366 the sphere-compression results, voxel models of the femur–acetabulum problem, created with side
367 length 1 mm ($a/R \sim 0.04$ for the whole femoral head), were expected to show significant errors in
368 bonded contact prediction especially at the near-surface regions. For the SC-SC and SS-SC models
369 relatively smaller errors were expected, with additional quantitative improvement expected for SS-
370 SC due to the lower dispersion in errors. However, close to the local features of high curvature
371 (where $a/R \sim 0.2$), it was expected that the errors in all contact models would be similar and high.
372 Yet, the prediction of the stress distributions throughout the femoral head interior by the SS-SC
373 formulation was found to be excellent, and was better than that by the SC-SC and bonded contact
374 formulations. This can be explained by the fact that the contact-induced stresses in the hip joint
375 problem influenced a much larger region around the points of contact than in the sphere compression
376 problem, leading to suppression of localized regions of large error. The benchmark results show that
377 the influence of contact was evident even at significant depths from the femoral head surface. This
378 explains why the relative performance improvement in the SS-SC formulation compared to the SC-
379 SC formulation (as evidenced by the global quantity NRMSE) was even better than that estimated
380 by the sphere compression results. The results from the bonded contact model, which represents the
381 state-of-the-art in μ FE, was found to be of very low quality throughout for this particular problem.
382 The inability to allow finite slipping led to tensile stresses at the contact boundary.

383 In the SC-SC and SS-SC models, the subset of slaves nodes that participate actively in contact (i.e.
384 possess a non-zero contact force magnitude) emerge automatically during the solution procedure.
385 Hence, considering a larger set of nodes as slave nodes initially does not affect the end result. This
386 is not the case for the bonded contact approach, as too many bonded nodes would cause larger
387 deviations in the result. In order not to artificially bias against the bonded result in this manner, we
388 selected the bonded nodes based on the initial gap distance between the femur and the pelvis. This
389 set of nodes was a smaller subset of the set of nodes defined as slave nodes in the SC-SC and SS-SC
390 femur models. In order to test that this subset was not too small, i.e. it did not omit locations that

391 would otherwise participate in contact, we analysed the SC-SC and SS-SC results *a posteriori*. It
392 was found that the slave nodes that were in active contact were a subset of the nodes defined as
393 bonded nodes, thereby assuring that the bonded model did not bond too few nodes.

394 The improvement in overall prediction accuracy going from the bonded contact model to the
395 SS-SC model makes a strong case for why the latter should be implemented within state-of-the-art
396 voxel-based μ FE software. It is interesting to note that, to the best of our knowledge, no FE software
397 package currently enables the customization of contact gap definition, i.e. the distance between a
398 slave node and its corresponding master surface element. This definition is central to the SS-SC
399 implementation, and its customizability should be considered in the design of contact analysis in FE
400 software packages.

401 The current implementation of the contact algorithm did not investigate the scenario when the
402 master surface is deformable assuming it to be rigid in both the sphere compression and femur–
403 acetabulum contact problems. This simplified the computation of the contact stiffness matrix terms
404 since changes to the master surface normal could be neglected. In the application area of bone
405 contact this assumption is reasonable, since the surfaces do not undergo large deformations and
406 any rigid body motion can be removed by choosing the coordinate system to move with the master
407 surface. However, numerical formulations of the additional contact stiffness matrix terms in the
408 presence of a deformable master surface are readily found in the literature [18] and do not limit the
409 implementation of the SS-SC formulation itself.

410 The constitutive behavior of the hemisphere and the femur were taken to be linear elastic
411 homogeneous and isotropic. Past studies have shown that in the context of bone contact interaction,
412 both elasticity and failure are important, and tension–compression non-linearity and anisotropy in
413 both moduli and strength are expected to play a role. It is obvious that accounting for the above
414 complexities will influence the accuracy and precision values estimated in this paper. Further studies
415 are needed to evaluate the effect of such considerations on voxel-based contact analysis which were
416 outside the scope of the present work.

417 In conclusion, a contact problem considered in this paper was that between a plane and a
418 sphere, the latter possessing a homogeneous curvature at all points of its 3D surface. Use of this
419 simple geometry removed confounding factors and enabled a thorough investigation of the effect
420 of orientation and mesh-refinement on the accuracy of stress prediction. The superiority of the SS-
421 SC formulation over the SC-SC and, in particular, the bonded contact formulations was shown
422 to be valid across a range of values of orientation and mesh-refinement that is relevant to bone
423 contact models. Subsequent to these findings, a realistic problem of femur–acetabulum contact
424 was further investigated. It was found that the reduction in errors going from the SC-SC model
425 to the SS-SC model was in fact much larger in this more realistic problem, than what was estimated
426 from the sphere compression results. This can be explained by the inherent differences in how
427 contact-induced stresses influence the solution between the realistic case and the simple problem.
428 Furthermore, it was shown that the improvement due to the SS-SC algorithm over the state-of-the-art
429 (bonded contact) was potentially even larger in realistic problems.

430 These findings demonstrate that the novel SS-SC formulation introduced in this paper can
431 significantly increase the current scope of application of voxel-based bone models, especially to
432 problems involving contact.

433 ACKNOWLEDGEMENTS

434
435 The authors would like to acknowledge funding from the Research Fund KU Leuven, Grant
436 STRT1/08/027. DB acknowledges his research stay at KU Leuven was made possible with the support
437 of the Erasmus Mundus programme of the European Union. The assistance of Mr Sujeet Phanse in using
438 the MATLAB function pcg (pre-conditioned conjugate gradients) to solve the very large DOF models is
439 acknowledged.

440 REFERENCES

- 441
442 1. van Rietbergen B. Micro-FE analyses of bone: State of the art. *Noninvasive Assessment of Trabecular Bone*
443 *Architecture and the Competence of Bone*, Majumdar S, Bay BK (eds.). Springer US: Boston, MA, 2001; 21–30,

- 444 doi:10.1007/978-1-4615-0651-5_3.
- 445 2. van Rietbergen B, Ito K. A survey of micro-finite element analysis for clinical assessment of bone strength: The
446 first decade. *Journal of Biomechanics* 2015; **48**(5):832–841, doi:10.1016/j.jbiomech.2014.12.024.
- 447 3. Wirth AJ, Müller R, van Lenthe GH. Computational analyses of small endosseous implants in osteoporotic bone.
448 *European Cells and Materials* 2010; **20**:58–71.
- 449 4. Flaig C, Arbenz P. A scalable memory efficient multigrid solver for micro-finite element analyses based on CT
450 images. *Parallel Computing* 2011; **37**(12):846–854, doi:10.1016/j.parco.2011.08.001.
- 451 5. Pistoia W, van Rietbergen B, Lochmüller EM, Lill CA, Eckstein F, Rüegsegger P. Image-based micro-finite-
452 element modeling for improved distal radius strength diagnosis: moving from bench to bedside. *Journal of Clinical*
453 *Densitometry* 2004; **7**:153–160, doi:10.1385/JCD:7:2:153.
- 454 6. Ito M. Assessment of bone quality using micro-computed tomography (micro-CT) and synchrotron micro-CT.
455 *Journal of Bone and Mineral Metabolism* 2005; **23**(1):115–121, doi:10.1007/BF03026335.
- 456 7. Colloca M, Blanchard R, Hellmich C, Ito K, van Rietbergen B. A multiscale analytical approach for bone
457 remodeling simulations: Linking scales from collagen to trabeculae. *Bone* 2014; **64**:303–313, doi:10.1016/j.bone.
458 2014.03.050.
- 459 8. Wirth AJ, Müller R, van Lenthe GH. The discrete nature of trabecular bone microarchitecture affects implant
460 stability. *Journal of Biomechanics* 2012; **45**:1060–1067, doi:10.1016/j.jbiomech.2011.12.024.
- 461 9. Arbenz P, Flaig C. On smoothing surfaces in voxel based finite element analysis of trabecular bone. *6th International*
462 *Conference on Large-Scale Scientific Computing*, Lirkov I, Margenov S, Waśniewski J (eds.). Springer: Berlin,
463 Heidelberg, 2008; 69–77, doi:10.1007/978-3-540-78827-0.
- 464 10. Boyd SK, Müller R. Smooth surface meshing for automated finite element model generation from 3D image data.
465 *Journal of Biomechanics* 2006; **39**:1287–1295, doi:10.1016/j.jbiomech.2005.03.006.
- 466 11. Camacho DL, Hopper RH, Lin GM, Myers BS. An improved method for finite element mesh generation of
467 geometrically complex structures with application to the skullbase. *Journal of Biomechanics* 1997; **30**:1067–1070,
468 doi:10.1016/S0021-9290(97)00073-0.
- 469 12. Wang ZL, Teo JCM, Chui CK, Ong SH, Yan CH, Wang SC, Wong HK, Teoh SH. Computational biomechanical
470 modelling of the lumbar spine using marching-cubes surface smoothed finite element voxel meshing. *Computer*
471 *Methods and Programs in Biomedicine* 2005; **80**:25–35, doi:10.1016/j.cmpb.2005.06.006.
- 472 13. Guldberg RE, Hollister SJ, Charras GT. The accuracy of digital image-based finite element models. *Journal of*
473 *Biomechanical Engineering* 1998; **120**:289–295, doi:10.1115/1.2798314.
- 474 14. Stadelmann VA, Conway CM, Boyd SK. In vivo monitoring of bone-implant bond strength by microCT and finite
475 element modelling. *Computer Methods in Biomechanics and Biomedical Engineering* 2011; **16**:993–1001, doi:
476 10.1080/10255842.2011.648625.
- 477 15. Steiner JA, Ferguson SJ, van Lenthe GH. Computational analysis of primary implant stability in trabecular bone.
478 *Journal of Biomechanics* 2015; **48**:807–815, doi:10.1016/j.jbiomech.2014.12.008.

- 479 16. Wirth AJ, Goldhahn J, Flaig C, Arbenz P, Müller R, van Lenthe GH. Implant stability is affected by local bone
480 microstructural quality. *Bone* 2011; **49**:473–478, doi:10.1016/j.bone.2011.05.001.
- 481 17. Hallquist JO, Goudreau GL, Benson DJ. Sliding interfaces with contact-impact in large-scale Lagrangian
482 computations. *Computer Methods in Applied Mechanics and Engineering* 1985; **51**:107–137, doi:10.1016/
483 0045-7825(85)90030-1.
- 484 18. Wriggers P. *Computational Contact Mechanics*. Second edn., Springer-Verlag: Berlin, Heidelberg, 2006, doi:
485 10.1007/978-3-540-32609-0.
- 486 19. Timoshenko S, Goodier JN. *Theory of Elasticity*. Second edn., McGraw-Hill Book Company: New York, 1951.
- 487 20. Zienkiewicz OC, Taylor RL, Zhu JZ. *The Finite Element Method*. Sixth edn., Butterworth-Heinemann: Oxford,
488 2005, doi:10.1016/B978-075066431-8.50165-X.
- 489 21. Zienkiewicz OC, Taylor RL, Fox D. *The Finite Element Method for Solid and Structural Mechanics*. Seventh edn.,
490 Butterworth-Heinemann: Oxford, 2014, doi:10.1016/B978-1-85617-634-7.00016-8.
- 491 22. Grosland NM, Brown TD. A voxel-based formulation for contact finite element analysis. *Computer Methods in*
492 *Biomechanics and Biomedical Engineering* 2002; **5**:21–32, doi:10.1080/10255840290032180.
- 493 23. The VAKHUM project public dataset. [http://www.ulb.ac.be/project/vakhum/public_dataset/
494 public-data.htm](http://www.ulb.ac.be/project/vakhum/public_dataset/public-data.htm). Accessed: 14 March 2017.
- 495 24. Van Sint Jan S. The VAKHUM project: virtual animation of the kinematics of the human. *Theoretical Issues in*
496 *Ergonomics Science* 2005; **6**(3–4):277–279, doi:10.1080/14639220412331529591.
- 497 25. Aitkenhead AH. Mesh voxelisation. [http://uk.mathworks.com/matlabcentral/fileexchange/
498 27390-mesh-voxelisation](http://uk.mathworks.com/matlabcentral/fileexchange/27390-mesh-voxelisation). Accessed: 14 March 2017.

Table I. Coordinates of the locations shown in Figure 1A.

	Loc-1	Loc-2	Loc-3	Loc-4	Loc-5	Loc-6	Loc-7
X/R	1.000	0.577	0.707	0.924	0.888	0.674	0.855
Y/R	0.000	0.577	0.000	0.000	0.325	0.303	0.216
Z/R	0.000	0.577	0.707	0.383	0.325	0.674	0.472

Table II. Comparison of normalized maximum absolute error (NMAXABSE) and normalized root mean squared error (NRMSE) in principal ($\sigma_1, \sigma_2, \sigma_3$), normal ($\sigma_{xx}, \sigma_{yy}, \sigma_{zz}$) and shear ($\sigma_{xy}, \sigma_{xz}, \sigma_{yz}$) stress fields for the bonded, stair-case, sliding contact (SC-SC) and simulated smoothed surface, sliding contact (SS-SC) formulations compared to the benchmark model of femur–acetabulum contact.

	NMAXABSE			NRMSE		
	Bonded	SC-SC	SS-SC	Bonded	SC-SC	SS-SC
σ_1	0.943	0.510	0.560	0.116	0.0291	0.00853
σ_2	0.941	0.540	0.511	0.153	0.0336	0.00817
σ_3	1.75	0.676	0.427	0.305	0.0409	0.00806
σ_{xx}	1.45	0.433	0.440	0.260	0.0387	0.00728
σ_{yy}	0.957	0.429	0.387	0.116	0.0290	0.00689
σ_{zz}	1.60	0.839	0.444	0.213	0.0299	0.00829
σ_{xy}	2.31	0.894	0.354	0.266	0.0436	0.00925
σ_{xz}	2.75	0.700	0.285	0.422	0.0473	0.0102
σ_{yz}	1.78	1.01	0.450	0.217	0.0496	0.0116

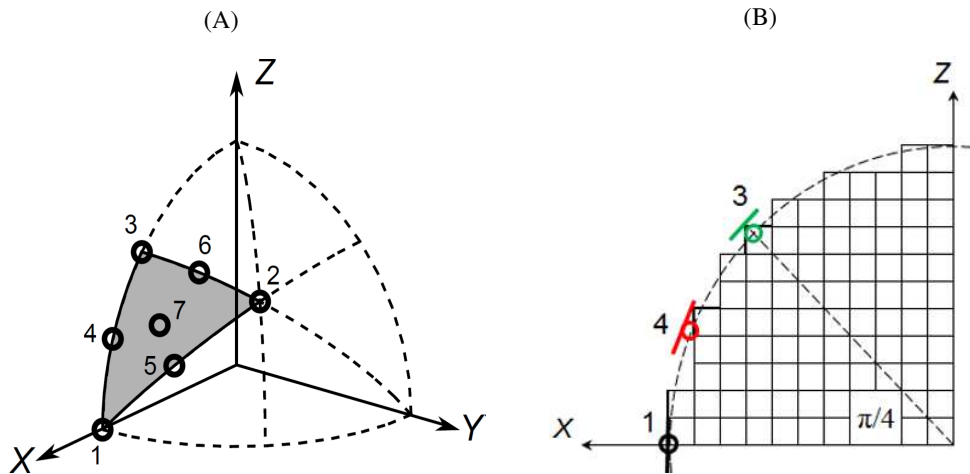


Figure 1. (A) The shaded triangular region is the smallest region on the spherical surface that presents unique orientations of the voxels to a local tangent plane. Seven locations on this shaded region are labeled Loc-1 to Loc-7. Dashed curves lie on symmetry planes about which the shaded region can be repeatedly reflected to recover the entire spherical surface. (B) Reflective symmetry can be visualized on the positive quadrant of the X - Z plane. Unique orientations of the voxels (solid outline) with respect to local tangents (coloured lines) are present entirely within the 45° -sector bounded by the locations Loc-1 and Loc-3.

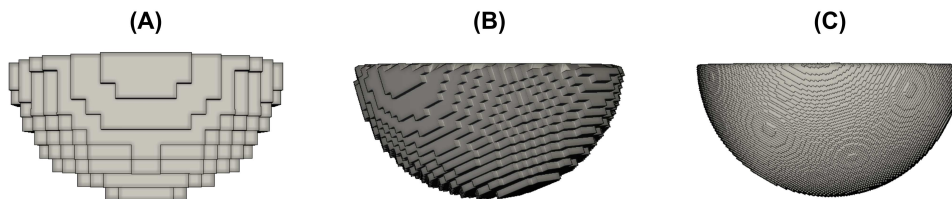


Figure 2. Mesh of the voxelated hemisphere for representative combinations of mesh-refinement and voxel orientation: (A) $a/R = 0.1$ and Loc-1, (B) $a/R = 0.05$ and Loc-4, (C) $a/R = 0.0125$ and Loc-7.

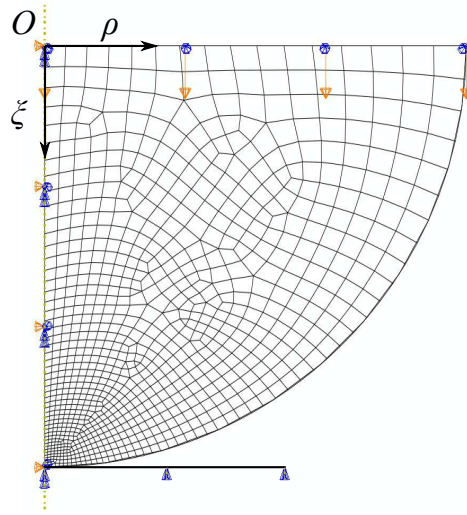


Figure 3. Mesh and applied boundary conditions for the benchmark model.

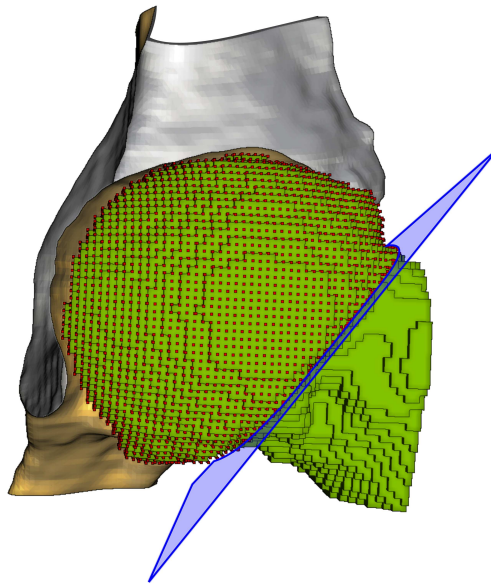


Figure 4. In the voxel models, contact interaction was defined between the outward pelvis surface facets (yellow) and the exterior nodes of the femur (red dots) that were on the acetabulum facing side of a specified plane (transparent blue). Here the pelvis is cut at a coronal cross-section to clarify the position of the acetabular surface with respect to the femoral head in the reference configuration.

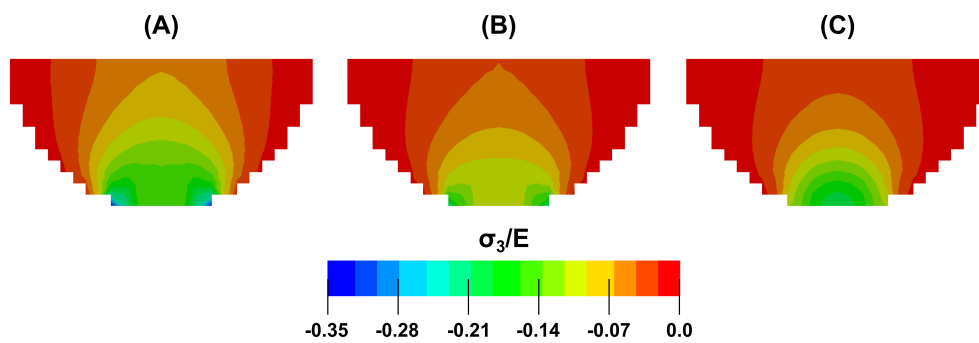


Figure 5. Contours of minimum principal stress computed by (A) bonded, (B) stair-case, sliding contact (SC-SC) and (C) simulated smoothed surface, sliding contact (SS-SC) models, respectively, are shown on the $y = 0$ plane of the hemispheres in the reference configuration, corresponding to $a/R = 0.075$ and Loc-1 case. Stress values are normalized with respect to the Young's modulus E .

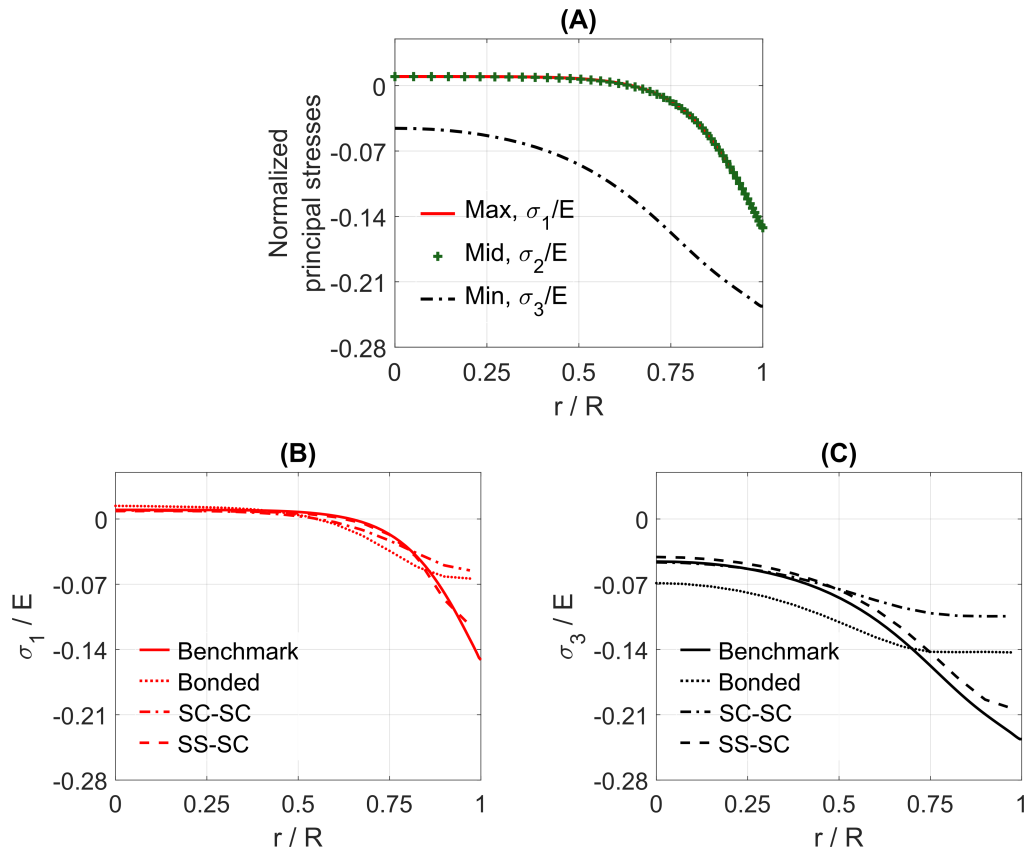


Figure 6. Principal stresses normalized with respect to Young's modulus E along the radial line passing through the point of initial contact. Normalized distances 0 and 1 correspond to the centre of the sphere and the point of initial contact, respectively. (A) Maximum, middle and minimum principal stresses in the benchmark model. For the voxel geometry corresponding to $a/R = 0.075$ and Loc-1, (B) maximum and (C) minimum principal stresses are compared with the benchmark for the bonded, stair-case, sliding contact (SC-SC) and simulated smoothed surface, sliding contact (SS-SC) models.

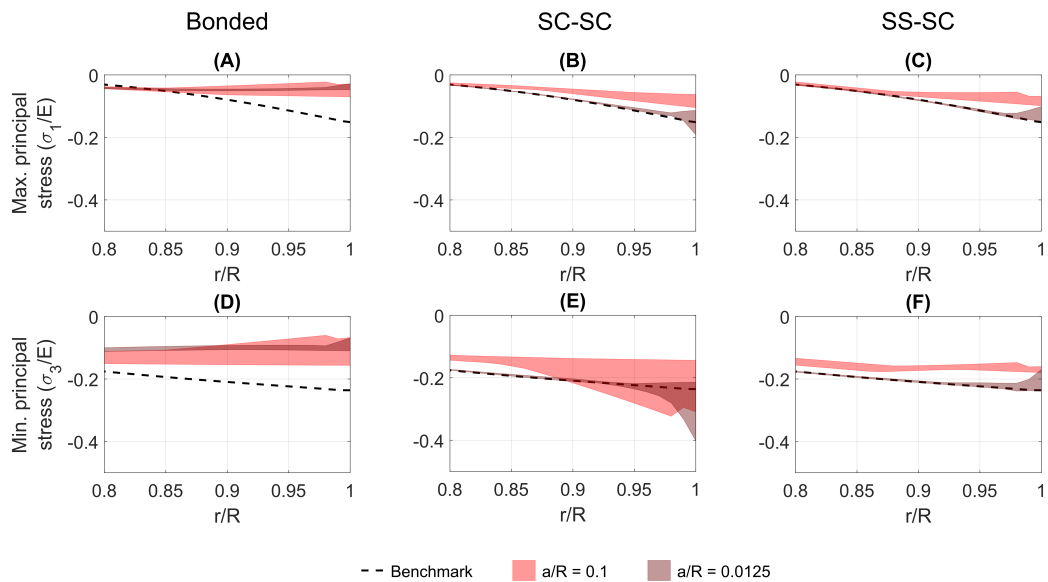


Figure 7. The influence of mesh refinement on the dispersion in predicted stresses across different voxel orientations for the bonded, stair-case, sliding contact (SC-SC) and simulated smoothed surface, sliding contact (SS-SC) models. Predicted stresses for the coarsest ($a/R = 0.1$) and the most refined ($a/R = 0.0125$) voxel models are shown. Stresses are normalized with respect to Young's modulus E and plotted along the undeformed radial line and in the region close to contact ($x \geq 0.8$). The shaded envelopes show the dispersion of predicted stresses across the different orientations. The dashed line is the stress predicted by the benchmark model.

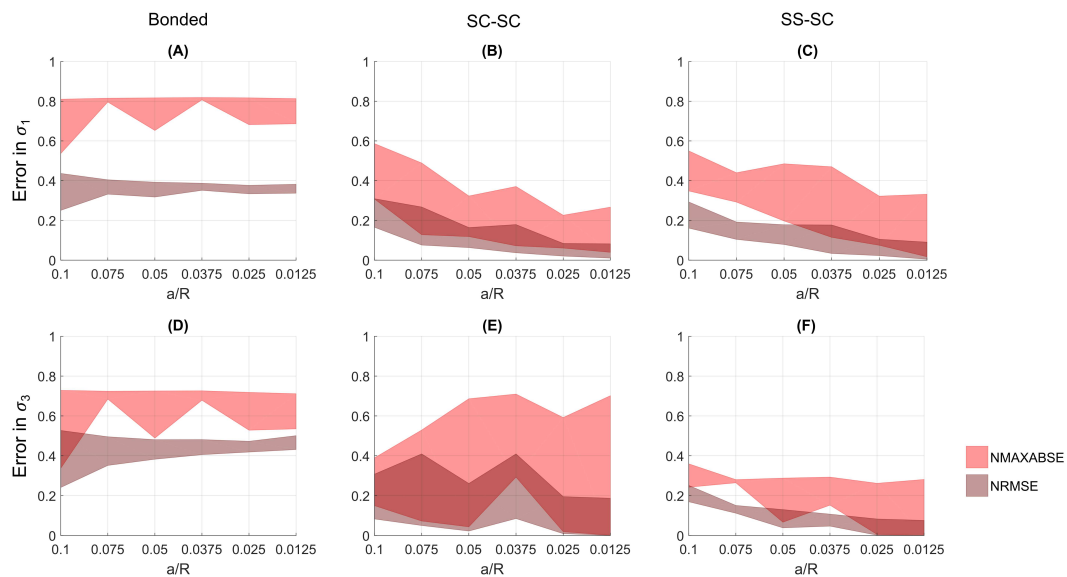


Figure 8. Comparison of normalized maximum absolute error (NMAXABSE) and normalized root mean squared error (NRMSE) in (A–C) maximum and (D–F) minimum principal stress predictions for the bonded, stair-case, sliding contact (SC-SC) and simulated smoothed surface, sliding contact (SS-SC) models. The shaded envelopes depict the dispersion of the errors across the different orientations over a range of mesh refinements.

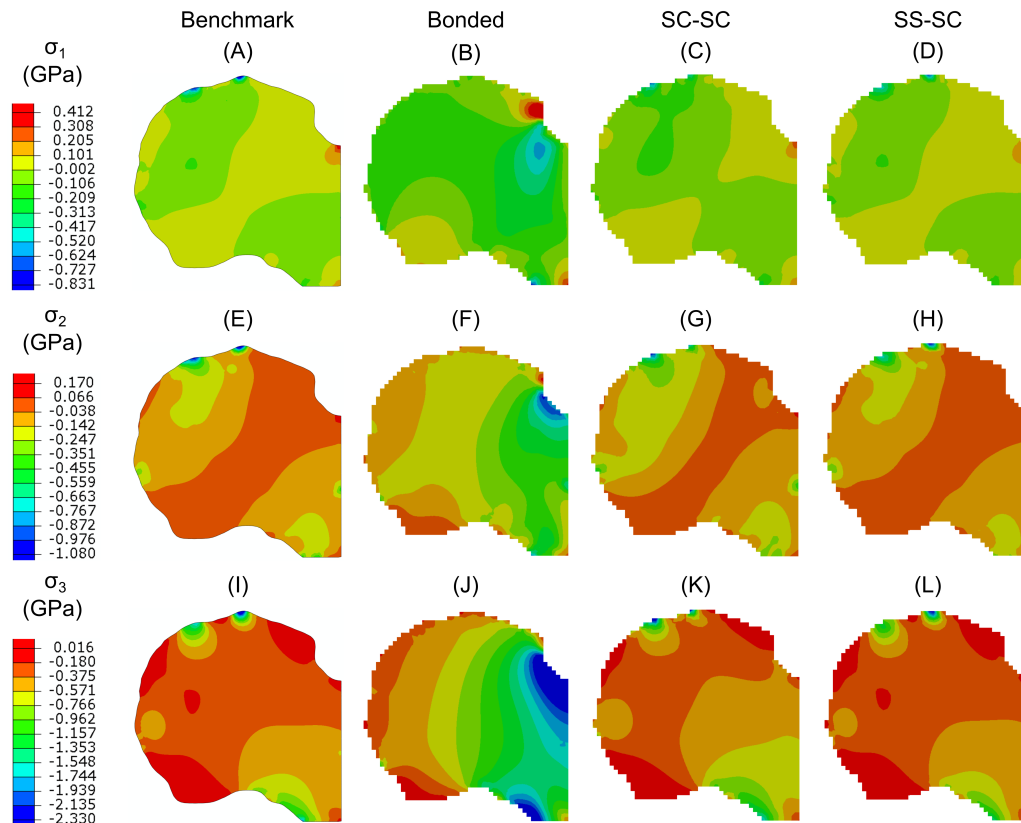


Figure 9. Comparison of principal stresses at the same coronal section between the tetrahedral mesh model (A,E,I), the voxel mesh model with bonded contact (B,F,J), stair-case, sliding contact or SC-SC (C,G,K) and simulated smoothed surface, sliding contact or SS-SC (D,H,L) formulations.